robots and create sharp edges; this resulted in a positive-feedback process where the sharp edges attracted more collisions, resulting in complex boundaries being formed as the initial group dissolved. Idealized mathematical models of robot swarms do not predict these phenomena.

Collective behavior in nature often involves large numbers of independent individuals interacting to produce complex assemblies. Engineered systems such as DNA-based self-assembly (27) have replicated this ability in synthesized chemical systems. We have demonstrated this ability in a robotic system by creating and programming a large-scale autonomous swarm to achieve complex global behavior from the cooperation of many limited and noisy individuals. The large-scale experiments advance our ability to engineer complex robotic systems. This motivates new investigations into advanced collective algorithms capable of detecting malfunctioning robots and recovering from large-scale external damages, as well as new robot designs that, like army ants, can physically attach to each other to form stable self-assemblages.

REFERENCES AND NOTES

1. G. M. Whitesides, B. Grzybowski, *Science* **295**, 2418–2421 (2002).
2. H. C. Berg, *Annu. Rev. Biochem.* **72**, 19–54 (2003).
3. P. Lawrence, *The Making of a Fly: The Genetics of Animal Design* (Blackwell, Oxford, 1992).
4. S. Camazine et al., *Self-Organization in Biological Systems* (Princeton Univ. Press, Princeton, NJ, 2003).
5. C. Anderson, G. Theraulaz, J. Deneubourg, *Insectes Soc.* **49**, 99–110 (2002).
6. N. J. Mlot, C. A. Tovey, D. L. Hu, *Proc. Natl. Acad. Sci. U.S.A.* **108**, 7669–7673 (2011).
7. M. Kirschner, J. Gerhart, *The Plausibility of Life: Resolving Darwin's Dilemma* (Yale Univ. Press, New Haven, CT, 2005).
8. R. Wood, R. Nagpal, G. Y. Wei, *Sci. Am.* **308**, 60–65 (March 2013).
9. R. Groß, M. Bonani, F. Mondada, M. Dorigo, *IEEE Trans. Robot.* **22**, 1115–1130 (2006).
10. E. William, G, Mermoud, A. Martinoli, in *Proceedings of the 2010 International Conference on Robotics and Automation* (Anchorage, AK, May 2010), pp. 1438–1445.
11. M. Yim et al., *Robot. Automat. Mag.* **14**, 43–52 (2007).
12. S. Goldstein, J. Campbell, T. Mowry, *Computer* **38**, 99–101 (2005).
13. M. Tolley, H. Lipson, *Int. J. Robot. Res.* **30**, 1566–1584 (2011).
14. P. Wurman, R. D'Andrea, M. Mountz, *AI Mag.* **29**, 9–19 (2008).
15. K. Konolige et al., *Exp. Robot.* **IX**, 131–140 (2006).
16. J. McLurkin et al., in *AAAI Spring Symposium: To Boldly Go Where No Human-Robot Team Has Gone Before* (Stanford, CA, March 2006), pp. 72–75.
17. M. Rubenstein, C. Ahler, R. Nagpal, in *Proceedings of the 2012 IEEE International Conference on Robotics and Automation* (St. Paul, MN, May 2012), pp. 3293–3298.
18. P. Vartholomeos, E. Papadopoulos, in *Proceedings of the 2006 IEEE International Conference on Robotics and Automation* (Orlando, FL, May 2006), pp. 649–654.
19. See supplementary materials on *Science* Online.
20. D. Moore, J. Leonard, D. Rus, S. Teller, in *The 2nd International Conference on Embedded Networked Sensor Systems* (Baltimore, November 2004), pp. 50–61.
21. J. Werfel, Y. Bar-Yam, D. Rus, R. Nagpal, in *Proceedings of the 2006 IEEE International Conference on Robotics and Automation* (Orlando, FL, May 2006), pp. 2787–2794.
22. D. Arbuckle, A. Requicha, *Auton. Robots* **28**, 197–211 (2010).
23. K. Støy, *Robot. Auton. Syst.* **54**, 135–141 (2006).
24. K. Tomita, S. Murata, H. Kurokawa, E. Yoshida, S. Kokaji, *IEEE Trans. Robot. Autom.* **15**, 1035–1045 (1999).
25. M. De Rosa, S. Goldstein, P. Lee, J. Campbell, P. Pillai, in *Proceedings of the 2006 IEEE International Conference on Robotics and Automation* (Orlando, FL, May 2006), pp. 1462–1468.
26. R. Nagpal, H. Shrobe, J. Bachrach, in *Information Processing in Sensor Networks*, F. Zhao, L. Guibas, Eds. (Springer, Berlin, 2003), pp. 333–348.
27. P. W. Rothemund, *Nature* **440**, 297–302 (2006).

RNA NANOSTRUCTURES

A single-stranded architecture for cotranscriptional folding of RNA nanostructures

Cody Geary,[1] Paul W. K. Rothemund,[2] Ebbe S. Andersen[1]*

Artificial DNA and RNA structures have been used as scaffolds for a variety of nanoscale devices. In comparison to DNA structures, RNA structures have been limited in size, but they also have advantages: RNA can fold during transcription and thus can be genetically encoded and expressed in cells. We introduce an architecture for designing artificial RNA structures that fold from a single strand, in which arrays of antiparallel RNA helices are precisely organized by RNA tertiary motifs and a new type of crossover pattern. We constructed RNA tiles that assemble into hexagonal lattices and demonstrated that lattices can be made by annealing and/or cotranscriptional folding. Tiles can be scaled up to 660 nucleotides in length, reaching a size comparable to that of large natural ribozymes.

Design methods for DNA (1, 2) and RNA (3–5) nanostructures have been developing along parallel lines for more than a decade. Both allow the generation of a wide variety of structures, including polygons (6–8), three-dimensional (3D) shapes (9–13), 1D arrays (3, 14), and 2D lattices (15, 16). RNA structure design lags behind only in the size of structures created: Whereas RNA designs have been limited to 50 to 200 nucleotides (nt), DNA structures up to 45,000 nt have been achieved (17, 18). The advantage of RNA structures lies in their greater potential to be cloned, genetically expressed in large quantities, and used for synthetic biology applications in vivo. DNA nanostructures built from single strands (19), or mostly single strands (9), have been synthesized or even cloned (20), but they variously require downstream purification or heat annealing, and none has yet been demonstrated to be folded isothermally as it is enzymatically produced.

RNA nanostructures have already been cotranscriptionally assembled from a mixture of numerous strands (12) and expressed in bacterial cells (21). Even if genetically encoded DNA structures are eventually achieved, other breakthroughs will have to be made, because existing DNA nanostructures lack the structural resolution and diversity of RNA tertiary motifs (22), such as kissing-loop interactions (KLs) (23), and they are currently unable to match the functional capacity of RNA to perform tasks such as scaffolding proteins (21, 24), detecting ligands (25), or releasing small interfering RNAs in response to stimuli (26). But despite the potential for expressible RNA structures, a general architecture for designing them has yet to be achieved.

We present a method for designing single-stranded RNA (ssRNA) structures that can fold either by heat-annealing over mica or by cotranscriptional folding. Similar to the previously reported scaffolded DNA origami method (17), our ssRNA origami architecture is scalable and follows systematic design rules, in this case based on 3D modeling of the A-form helix. We demonstrated constructions up to six helices tall and 660 nt in length. We took inspiration from multistranded DNA double-crossover (DX) molecules (27) and their use as modular lattice-forming tiles (16). To turn multistranded DNA tiles into ssRNA ones, we developed an architecture that uses hairpins and programmable kissing loops. To extend the architecture to more than two helices, we introduced a new crossover pattern that we call a "dovetail seam, for creating arrays of coaxially stacked helices that are both sequence-specific and nontopologically linked.

Our design method used 3D modeling of RNA (Fig. 1A) to plan the interconnection of helices and RNA structural motifs to form compact structures and lattices (Fig. 1B). Outputs of 3D

[1]Center for DNA Nanotechnology, Interdisciplinary Nanoscience Center, and Department of Molecular Biology and Genetics, Aarhus University, 8000 Aarhus, Denmark. [2]Bioengineering, Computer Science, and Computation and Neural Systems, California Institute of Technology, Pasadena, CA 91125, USA.
*Corresponding author. E-mail: esa@inano.au.dk

modeling were used to produce secondary structure blueprints (Fig. 1C), to which sequences were assigned by sequence design algorithms so that the structures could be synthesized and tested by one of two experimental protocols (Fig. 2, B and C). Figure 1D shows the vision that guided our design of RNA structures for cotranscriptional folding: RNA structures should contain stable hairpins that fold up in the order they are produced by the polymerase (Fig. 1D, 1 to 4). Next, the hairpins should condense in a sequential fashion dictated by long-range interactions (Fig. 1D, 5 to 7) to create a global fold. Finally, individual structures may assemble further into higher-order quaternary structures (Fig. 1D, 8). In all our designs, we specified the start of transcription (the 5′ end) to divide each structure into two independently and sequentially folding domains (Fig. 1D, inset).

RNA DX molecules were modeled by inserting crossovers between aligned computer-generated A-form RNA helices. By varying the spacing between the two antiparallel crossovers, we generated "antiparallel odd" (RNA-AO, Fig. 1A, top) or "antiparallel even" (RNA-AE, Fig. 1A, bottom) juxtapositions of the crossovers (27), where odd and even refer to the number of helical half-turns between crossovers. Similar to their DNA analogs (16), multistranded RNA-AE tiles comprise five different strands, whereas multistranded RNA-AO tiles comprise only four different strands. Unlike B-form DNA helices, which have only approximately –1° of base-pair inclination with respect to the helical axis (28), A-form RNA helices have approximately 19° of inclination (29) [fig. S1 (30)], accentuating a geometric difference between RNA-AE and RNA-AO tiles. In RNA-AE tiles, the base-pair inclinations of both helices align, and the base pairs between crossovers define a parallelogram (Fig. 1A, bottom). In contrast, in RNA-AO tiles the base-pair inclinations are opposed, so that the base pairs between crossovers define a trapezoid (Fig. 1A, top), and the number of base pairs between the crossovers on each helix is unequal.

Conversion of multistranded RNA DX tiles to ssRNA origami tiles (Fig. 1C) was accomplished by (i) connecting outer helix ends with hairpin loops and (ii) replacing one of the intercrossover helical domains with a 180° KL interaction. Depending on the sequence signature used [fig. S2 (30)], RNA KL interactions can define a wide variety of angles for construction, including ~180° connections (31) or ~120° bends (32) [Fig. 1B, insets; angles vary with sequence and exhibit some variation because of structural flexibility (33)]. The geometry of tile-tile interactions can be programmed by the choice of loops at the four corners of the tile. For example, by using six different 120° KL interactions, three different tiles can be programmed to form a hexagonal lattice (Fig. 1B). Alternatively, by using four different 180° KL interactions, two different tiles can be programmed to form a rectilinear lattice (Fig. 3D, top).
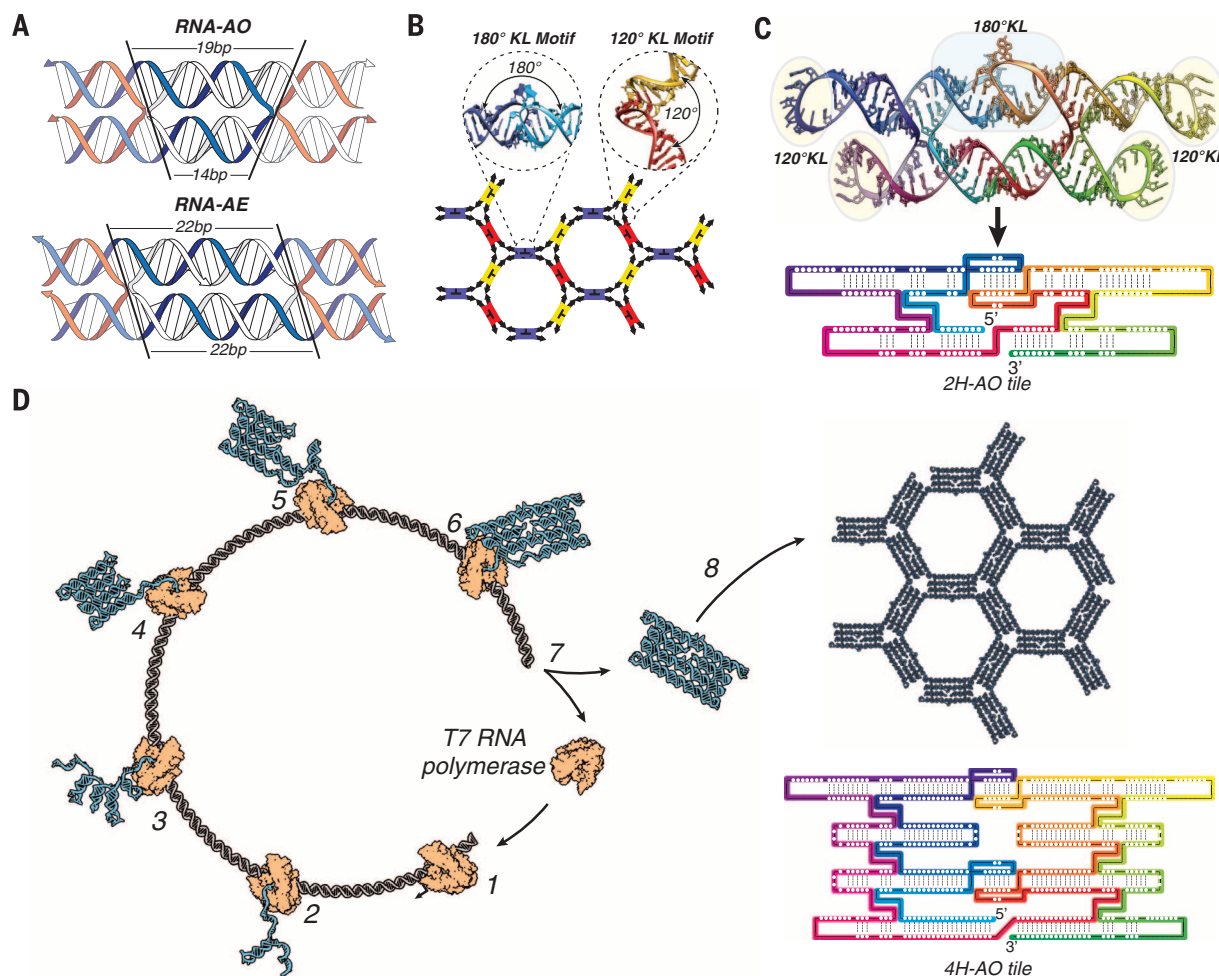

Fig. 1. Design of ssRNA origami for tile assembly. (A) Comparison of A-form antiparallel DX molecules: RNA-AO with an odd number of half-turns (three) between crossovers and RNA-AE with an even number (four). Base pairs between the crossovers of an RNA-AO define a trapezoid; those of an RNA-AE define a parallelogram. (B) Schematic shows how KL interactions of 180° (tile edges and left inset) and 120° (black arrows and right inset) can be used to specify a hexagonal lattice. (C) Design of a 2H-AO tile starts with 3D modeling from which a secondary structure blueprint is derived. The strand path is colored by a gradient that indicates the order of synthesis. (D) Schematic showing the cotranscriptional folding pathway for the 4H-AO tile. The T7 RNA polymerase binds to the template DNA (step 1) and the RNA folds as it is being synthesized (steps 2 to 6). By step 4, the 5′ half of the tile is fully synthesized and can fold into a domain composed of 11 helical subdomains. As the second domain is synthesized, the kissing loops can form in succession (steps 5 and 6). At the end of the synthesis (step 7), the tile is released and can form lattices (step 8).

Starting from the basic RNA-AO and RNA-AE geometries, tiles of different sizes were modeled using Assemble2 (*34*). Assemble2 generates A-RNA helices based on classical parameters (*35*) and helps to merge them with RNA tertiary motifs from the Protein Data Bank (PDB) [Fig. 2A, see materials and methods for details and PDB IDs (*30*)]. Two-helix structures (2H-AE and 2H-AO) were modeled on the initial RNA-AE and RNA-AO tiles shown in Fig. 1A. Taller four-helix (4H) and six-helix (6H) structures were generated, with an additional helical turn (11 base pairs) between crossovers that made them wider. Intra-tile 180° KLs were examined for steric clashes between AA bulges (a feature of the 180° KLs) and neighboring helices. Clashes predicted for 4H-AO and 6H-AO tiles motivated the omission of intra-tile KLs for every other helix. Inter-tile 120° KLs were
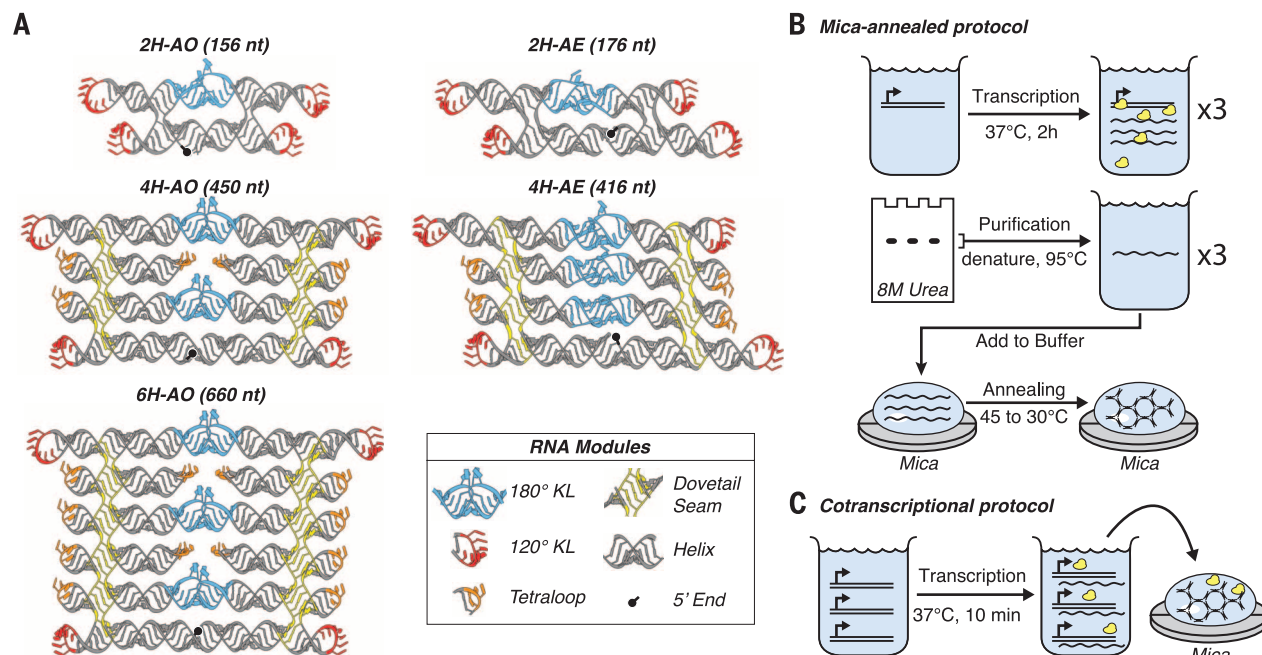

Fig. 2. ssRNA origami tiles and preparation protocols. (**A**) Renderings based on atomic models for RNA-AE and RNA-AO tiles that are two, four, and six helices tall. The legend shows structural modules. (**B**) Purification and annealing protocol showing DNA templates (double line), T7 promoter (bent arrows), T7 polymerase (yellow), RNA transcripts (wavy lines), and tile assembly. (**C**) Cotranscriptional folding protocol.

Fig. 3. Programming RNA tile assembly with KL interactions. (**A** to **D**, top) Schematics of different tile assemblies. (**A** to **D**, bottom) AFM images at two different zoom levels. (**A**) A single-tile 2H-AE system with 120° KLs forms hexagonal lattices. (**B**) A single-tile 2H-AO system with 120° KLs forms hexagonal lattices, but some defects are observed. (**C**) A two-tile 2H-AO system created by removing one of the tiles from a three-tile system (Fig. 1B) forms 1D zigzag arrays. (**D**) A two-tile 2H-AE system using 180° KLs forms rectilinear lattices. Samples were prepared as in Fig. 2B. Scale bars, 100 nm.
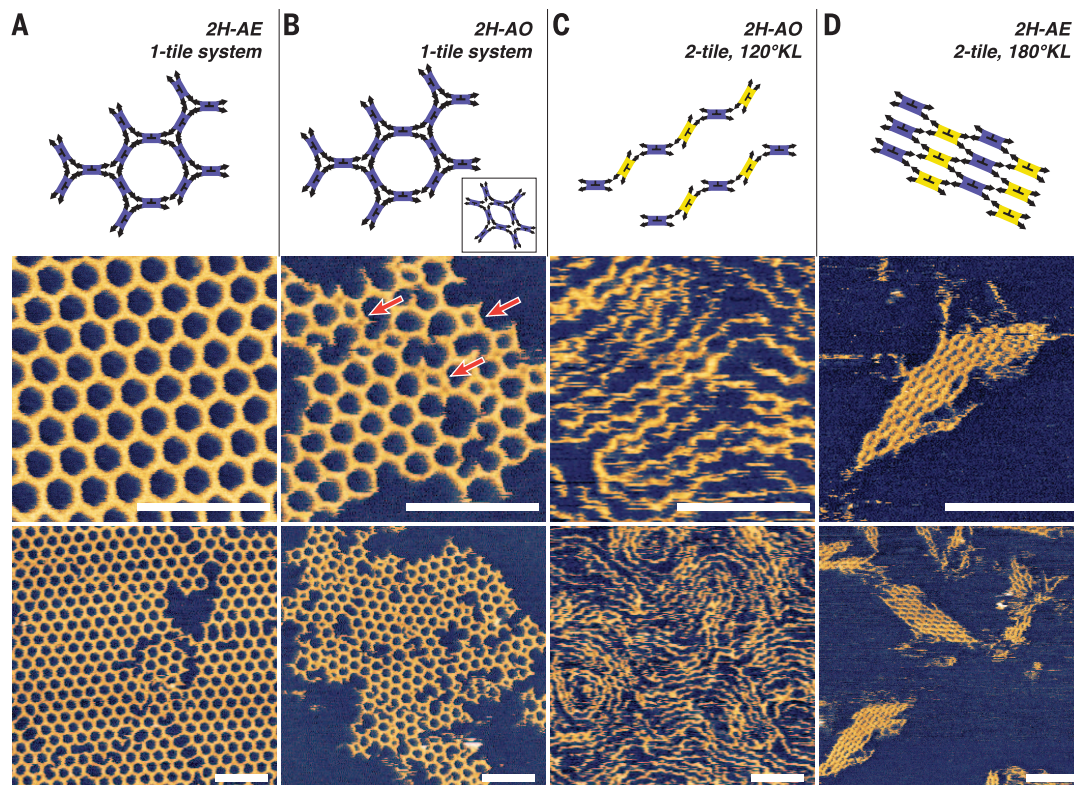
fit to tile corners (Fig. 2A, red module) by (i) rotating tiles (without corner KLs) using D_3 symmetry in UCSF Chimera molecular modeling software (36), (ii) arranging the tiles to form a planar structure, and (iii) aligning the nuclear magnetic resonance structure of the 120° KL between the tiles [materials and methods and fig. S3 (30)]. All helices not capped with KLs were terminated with GNRA or UNCG tetraloops (Fig. 2A, orange module) to increase thermostability (37).

For tiles more than two helices tall, crossovers form extended seams that the RNA backbone does not cross. Similar seams held together purely by stacking interactions have been created in DNA structures (17, 38), but they are not sequence-specific. By analogy with dovetail joints from woodworking, we introduced "dovetail seams" (Fig. 2A, yellow module) in which 2 to 3 base pairs cross the seam at each helix, providing sequence specificity and potentially aiding in the folding of the tile. Further, the number of base pairs in the dovetail seam can, in principle, be

used to control the geometry of the tile. In the 4H-AE tile, repeated use of a 2–base-pair dovetail should create slight curvature in the tile. In contrast, for the 4H-AO and 6H-AO tiles, 3–base-pair dovetails should cause each half of the tile to bend in opposite directions and impose a symmetry that tends to flatten the tile.

Secondary structures describing base pairing and strand paths were generated from 3D designs and represented in a simple text-based format. In principle, any position along the strand path could have been chosen as the start site for transcription. To avoid kinetic trapping (39), we positioned the 5′ start site and 3′ end to divide each tile into two domains, bridged by the 180° KLs [figs. S4 and S5 (30)]. In particular, this was intended to ensure that the folding of an entire domain precedes the formation of any KL interactions. Sequences for the RNA tiles were generated with NUPACK (40), aided by a Perl script [fig. S6 and note S2 (30)] that converts secondary structure into NUPACK's design format. Because secondary structure in the DNA template (from

which an RNA tile is transcribed) can interfere with the synthesis of that template, we designed sequences that would have less structure in their DNA form by adding G-U wobbles to our RNA tile designs, with a frequency of one wobble pair per every eight base pairs of helix [figs. S6 and S7 (30)]. The sequences of the 120° and 180° KL interactions were chosen because they are highly sequence-specific (8, 13) [fig. S8 and table S1 (30)].

To confirm the overall geometry of RNA-AO and RNA-AE DX tiles, we first explored them in the context of simple systems programmed to create hexagonal lattices from a single type of tile, which requires only two different KL interactions: The top left loop pairs with the bottom left loop and the top right loop pairs with the bottom right loop (Fig. 3, A and B, top). We first studied substrate-assisted lattice formation of purified tiles by annealing them over mica [materials and methods, Fig. 2B, and fig. S9 (30)], a process known to create micrometer-sized lattices of tiles that form only small lattices in solution (41, 42). Atomic force microscopy (AFM) revealed high
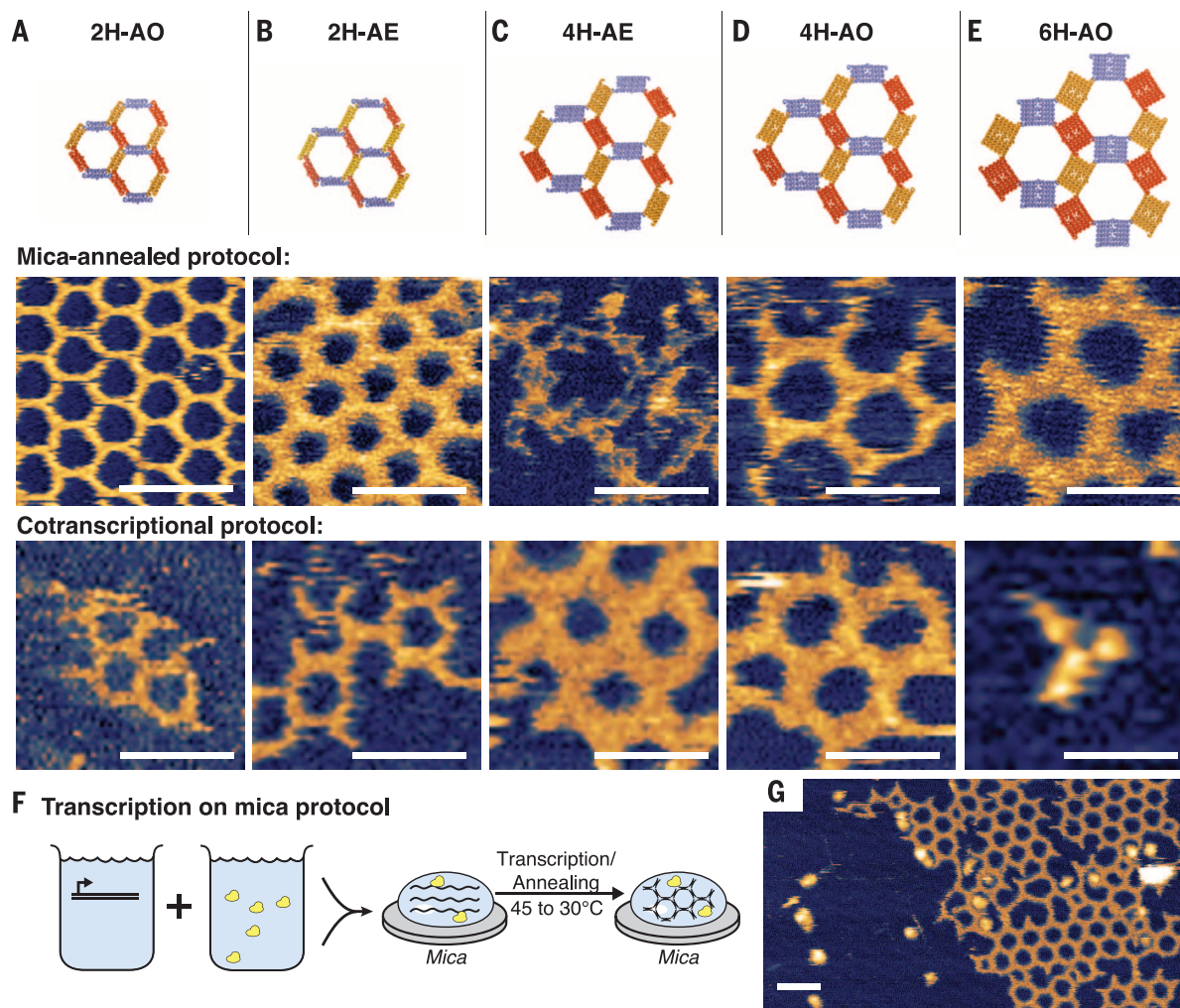

Fig. 4. Scalability of ssRNA tile architecture. (**A** to **E**) Three-tile hexagonal lattices shown in order of increasing tile size. (Top) 3D models displayed to scale. (Middle) AFM images of purified tiles annealed over mica as in Fig. 2B. (Bottom) AFM images of the same designs formed cotranscriptionally in solution and deposited on mica as in Fig. 2C. (**F**) Protocol for RNA transcription over mica, representing a combination of Fig. 2, B and C. (**G**) AFM images of 2H-AE tiles both transcribed and assembled directly over a mica surface. Scale bars, 50 nm.

surface coverage of the mica by 2H-AE and 2H-AO lattices (Fig. 3, A and B, bottom row), confirming that the basic geometry of these tiles and lattices was as designed. Defects in 2H-AE lattices, such as diamond-shaped cells or elongated eight-tile hexagons, occurred mainly at boundaries between ~300-nm crystal domains [Fig. 3A and fig. S10 (30)], whereas 2H-AO crystal domains were smaller (50 nm) and exhibited a number of nonhexagonal defects [Fig. 3B and fig. S11 (30)]. This result suggested that 2H-AO tiles have a slight distortion from the geometry predicted or may be more flexible than 2H-AE tiles. A control experiment in which two 2H-AO tiles were programmed to form 1D zigzag arrays (Fig. 3C) demonstrated that 120° KLs were at least successful in controlling the gross orientation of 2H-AO tiles. To demonstrate the geometric programmability of the tiles, we designed 2H-AE tiles of the same basic design demonstrated in Fig. 3A, but with 180° KLs for tile-tile connections [figs. S7 and S8 (30)]. As intended, these tiles formed rectilinear lattices (Fig. 3D) that were ~100 nm in size. We also examined the quality of solution-formed lattices by incubating a three-tile system 2H-AO at 37°C [materials and methods and fig. S9 (30)] and depositing the mixture over mica after assembly [fig. S12 (30)]. We observed fewer, smaller crystals than could be obtained by mica annealing of the same system (Fig. 4A, middle row).

To test the scalability of our architecture, we generated four-helix 4H-AO and 4H-AE tiles that are approximately 2.5 times greater in molecular weight than corresponding two-helix tiles, and six-helix 6H-AO tiles that are 4.2 times larger than corresponding two-helix tiles. Results from single-tile systems based on larger tiles (4H-AO and 4H-AE) were poor (a low yield of small lattices), but three-tile systems for all tile sizes (Fig. 4, top row) generated lattices by at least one of two different protocols: mica annealing (Fig. 4, middle row, and Fig. 2B) and cotranscriptional assembly at 37°C (Fig. 4, bottom row, and Fig. 2C). [See fig. S9 for protocols, fig. S13 for polyacrylamide gel electrophoresis gels, and figs. S14 to S21 for larger AFM views and height analysis showing that experimentally observed lattice spacings match predicted spacings within 2 nm, summarized in table S2 (30).]

Mica annealing yielded lattices in all cases except the 4H-AE system (Fig. 4C, middle row), which formed a disordered weblike structure. Gel electrophoresis of individual 4H-AE tiles solution-incubated at 37°C [fig. S13 (30)] showed that little or no monomer formed, and slower-migrating potentially misfolded species dominated. The sudden introduction of salt (upon which KL formation depends) to highly concentrated tiles occurs in both mica annealing and solution incubation protocols, and so in both cases 4H-AE tiles may have been kinetically trapped in multistranded structures, perhaps involving intermolecular binding of the strong 180° KLs intended as intramolecular contacts. However, cotranscriptional assembly of the 4H-AE system allowed small lattices to form (Fig. 4C, bottom row), and a sub-

stantial fraction of monomer was observed by gel electrophoresis of cotranscriptionally folded tiles [fig. S13 (30)].

Cotranscriptional assembly yielded lattices in all cases except the 6H-AO system (Fig. 4, A to E, bottom row). In this case, a substantial fraction of slower-migrating potentially misfolded tiles were observed by gel for both cotranscriptionally folded and solution-incubated tiles [fig. S13 (30)]. If all internal 180° KLs and the dovetail seams form as desired, a relatively flat tile would be created. However, given the symmetry and dovetail spacing used, the desired fold for the 6H-AO system may be highly strained, and it is possible for it to be trapped in more 3D distorted states of lower strain. This result is consistent with the increased height (~3.5 nm versus 2 to 2.5 nm for tiles in typical lattices) observed for cotranscriptionally assembled 6H-AO tiles [fig. S21 (30)]. In the case of mica annealing, the confinement and heating of 6H-AO tiles on the mica may have flattened tiles and allowed them to form lattices [Fig. 4E, middle row, and figs. S20 and S23 (30)]. This difference seems plausible because highly curved DNA tubes are slowly opened and flattened by interaction with mica surfaces (43). Combining the transcription of 2H-AE tiles with our mica annealing protocol (Fig. 4F) allowed the visualization of RNA polymerase in association with the tile lattice (Fig. 4G and fig. S22) and yielded our best cotranscriptional result.

We have shown that our ssRNA architecture is compatible with cotranscriptional folding and lattice assembly for four out of five tile designs tested. One design, the 4H-AE system, appeared to benefit from or perhaps require cotranscriptional folding. Figure 1D outlines how we envision how cotranscriptional folding proceeds for our architecture, diagrammed for the similar 4H-AO system. T7 RNA polymerase adds nucleotides quickly, in the range of 200 to 400 nt/s, and secondary structure forms two to three orders of magnitude more quickly, on the microsecond time scale (44, 45). Thus, we expect that halfway through transcription, the 5′ half of the tile will already be folded and the left half of each intramolecular KL will be positioned at the end of a helical stem. As the 3′ half of the tile is synthesized, the remaining halves of each intramolecular KL are expected to be synthesized and bind their complementary halves in order. Without such a prescribed ordering of folding, hairpins that we intend to form intramolecular KLs might have the opportunity to form intermolecular KLs and thus unintended multimeric structures, as might happen for 4H-AE tiles when not cotranscriptionally folded, perhaps because of their three somewhat crowded intramolecular KL interactions.

The 6H-AO tile artificial RNA nanostructure produced as a single strand comprises 660 nt and 35 helical subdomains, which corresponds to a structural complexity (4) comparable to that of the group II intron [fig. S24 (30)]. Although the basic architecture we present only provides for 2D structures, the addition of RNA modules that can control helical stacking, such as the A-minor four-way junction (46), or control bend-

ing such as the kink turn (47), could extend the architecture to three dimensions. More generally, augmentation of the basic architecture with complex tertiary motifs will allow structures with different geometry, finer detail, and specific protein binding (48).

REFERENCES AND NOTES

1. N. C. Seeman, J. Theor. Biol. 99, 237–247 (1982).
2. A. V. Pinheiro, D. Han, W. M. Shih, H. Yan, Nat. Nanotechnol. 6, 763–772 (2011).
3. L. Jaeger, N. B. Leontis, Angew. Chem. Int. Ed. Engl. 39, 2521–2524 (2000).
4. W. Grabow, L. Jaeger, F1000Prime Rep. 5, 46 (2013).
5. J. Lee et al., Proc. Natl. Acad. Sci. U.S.A. 111, 2122–2127 (2014).
6. I. Severcan, C. Geary, E. Verzemnieks, A. Chworos, L. Jaeger, Nano Lett. 9, 1270–1277 (2009).
7. P. Guo, C. Zhang, C. Chen, K. Garver, M. Trottier, Mol. Cell 2, 149–155 (1998).
8. W. W. Grabow et al., Nano Lett. 11, 878–887 (2011).
9. J. H. Chen, N. C. Seeman, Nature 350, 631–633 (1991).
10. W. M. Shih, J. D. Quispe, G. F. Joyce, Nature 427, 618–621 (2004).
11. E. S. Andersen et al., Nature 459, 73–76 (2009).
12. K. A. Afonin et al., Nat. Nanotechnol. 5, 676–682 (2010).
13. I. Severcan et al., Nat. Chem. 2, 772–779 (2010).
14. H. Yan, X. Zhang, Z. Shen, N. C. Seeman, Nature 415, 62–65 (2002).
15. A. Chworos et al., Science 306, 2068–2072 (2004).
16. E. Winfree, F. Liu, L. A. Wenzler, N. C. Seeman, Nature 394, 539–544 (1998).
17. P. W. K. Rothemund, Nature 440, 297–302 (2006).
18. B. Wei, M. Dai, P. Yin, Nature 485, 623–626 (2012).
19. Z. Li et al., J. Am. Chem. Soc. 131, 13093–13098 (2009).
20. C. Lin et al., Proc. Natl. Acad. Sci. U.S.A. 105, 17626–17631 (2008).
21. C. J. Delebecque, A. B. Lindner, P. A. Silver, F. A. Aldaye, Science 333, 470–474 (2011).
22. L. Jaeger, A. Chworos, Curr. Opin. Struct. Biol. 16, 531–543 (2006).
23. S. Horiya et al., Chem. Biol. 10, 645–654 (2003).
24. H. Ohno et al., Nat. Nanotechnol. 6, 116–120 (2011).
25. J. S. Paige, T. Nguyen-Duc, W. Song, S. R. Jaffrey, Science 335, 1194 (2012).
26. L. M. Hochrein, M. Schwarzkopf, M. Shahgholi, P. Yin, N. A. Pierce, J. Am. Chem. Soc. 135, 17322–17330 (2013).
27. T. J. Fu, N. C. Seeman, Biochemistry 32, 3211–3220 (1993).
28. R. E. Dickerson et al., Science 216, 475–485 (1982).
29. Y. Tanaka et al., Nucleic Acids Res. 27, 949–955 (1999).
30. See the supplementary materials on Science Online.
31. E. Ennifar, P. Walter, B. Ehresmann, C. Ehresmann, P. Dumas, Nat. Struct. Biol. 8, 1064–1068 (2001).
32. A. J. Lee, D. M. Crothers, Structure 6, 993–1007 (1998).
33. W. Kasprzak, E. Bindewald, T. J. Kim, L. Jaeger, B. A. Shapiro, Methods 54, 239–250 (2011).
34. S. Arnott, D. W. Hukins, S. D. Dover, W. Fuller, A. R. Hodgson, J. Mol. Biol. 81, 107–122 (1973).
35. F. Jossinet, T. E. Ludwig, E. Westhof, Bioinformatics 26, 2057–2059 (2010).
36. E. F. Pettersen et al., J. Comput. Chem. 25, 1605–1612 (2004).
37. M. Molinaro, I. Tinoco Jr., Nucleic Acids Res. 23, 3056–3063 (1995).
38. X. C. Bai, T. G. Martin, S. H. Scheres, H. Dietz, Proc. Natl. Acad. Sci. U.S.A. 109, 20012–20017 (2012).
39. H. Isambert, Methods 49, 189–196 (2009).
40. J. N. Zadeh et al., J. Comput. Chem. 32, 170–173 (2011).
41. X. Sun, S. Hyeon Ko, C. Zhang, A. E. Ribbe, C. Mao, J. Am. Chem. Soc. 131, 13248–13249 (2009).
42. S. Hamada, S. Murata, Angew. Chem. Int. Ed. Eng. 48, 6820–6823 (2009).
43. P. W. K. Rothemund et al., J. Am. Chem. Soc. 126, 16344–16352 (2004).
44. S. L. Heilman-Miller, S. A. Woodson, RNA 9, 722–733 (2003).
45. J. A. Cruz, E. Westhof, Cell 136, 604–609 (2009).
46. C. Geary, A. Chworos, L. Jaeger, Nucleic Acids Res. 39, 1066–1080 (2011).

47. D. J. Klein, T. M. Schmeing, P. B. Moore, T. A. Steitz, *EMBO J.* **20**, 4214–4221 (2001).
48. W. W. Grabow, L. Jaeger, *Acc. Chem. Res.* **47**, 1871–1880 (2014).

PHOTOSYNTHESIS

Electronic structure of the oxygen-evolving complex in photosystem II prior to O-O bond formation

Nicholas Cox,[1]* Marius Retegan,[1] Frank Neese,[1] Dimitrios A. Pantazis,[1] Alain Boussac,[2] Wolfgang Lubitz[1]*

The photosynthetic protein complex photosystem II oxidizes water to molecular oxygen at an embedded tetramanganese-calcium cluster. Resolving the geometric and electronic structure of this cluster in its highest metastable catalytic state (designated S_3) is a prerequisite for understanding the mechanism of O-O bond formation. Here, multifrequency, multidimensional magnetic resonance spectroscopy reveals that all four manganese ions of the catalyst are structurally and electronically similar immediately before the final oxygen evolution step; they all exhibit a 4+ formal oxidation state and octahedral local geometry. Only one structural model derived from quantum chemical modeling is consistent with all magnetic resonance data; its formation requires the binding of an additional water molecule. O-O bond formation would then proceed by the coupling of two proximal manganese-bound oxygens in the transition state of the cofactor.

In oxygenic photosynthesis, an inorganic Mn_4O_5Ca cofactor embedded in photosystem II (PSII) (Fig. 1A) catalyzes water oxidation to O_2 with a high turnover number (10^6) and a maximal turnover frequency (TOF) of ≈500 s^{-1} (*1*). In contrast, free Mn_xO_yCa oxides display intrinsically slow water-splitting capacity, with TOFs six orders of magnitude lower (*2*). The cofactor's reaction cycle comprises five distinct redox intermediates, the S_n states, where the subscript indicates the number of stored oxidizing equivalents (n = 0 to 4) required to split two water molecules (Fig. 1B) (*3*). The cycle is sequentially driven by the photo-oxidant of PSII (P680), a multichlorophyll pigment assembly. The photochemistry of the reaction center is coupled to the reaction catalyzed by the Mn_4O_5Ca cofactor via a nearby redox-active tyrosine residue Y_Z (D_1-Y161), which acts as a single electron gate (Fig. 1B). Upon the last oxidation of Y_Z, (forming the $S_3Y_Z^{\bullet}$ state), the system rapidly decays to the S_0 state, with the concomitant release of molecular triplet oxygen and the rebinding of one substrate water molecule (*4, 5*). The chemical steps involved in O-O bond formation in the transition state (S_4) remain uncertain.

The current molecular-level picture of the biological water-oxidizing catalyst extends only halfway through its reaction cycle, to the S_2 state. Here, the net oxidation states of the four manganese (Mn) ions are generally considered to be IV, IV, IV, and III (Fig. 1B); however, some researchers favor a net oxidation level two electrons lower: IV, III, III, and III [a discussion is available in (*1*)]. Theoretical models for the cofactor in the S_2 state (*6*), which combine structural (*7, 8*) and spectroscopic data (*9, 10*), suggest

that the cofactor in this state is inherently flexible. The cofactor adopts two distinct but interconvertible Mn core topologies, an open and a closed cubane motif, which differ by the reorganization of a single μ-oxo bridge, O5 (*6*), rendering the Mn^{III} ion five-coordinate.

Unlike the S_2 state, the structure of the S_3 state remains unresolved. Interpretation of x-ray spectroscopic data of S_3 is vigorously debated, with some researchers suggesting that its formation is accompanied by a Mn-centered oxidation, whereas others instead favor a ligand-centered oxidation, possibly of one of the substrate waters (Fig. 1B) (*11, 12*). Similarly, there is little agreement on the coordination number of the four Mn ions, or the number of substrate waters (1 or 2) bound to the cofactor before the S_3 state (*4, 5, 13*). This ambiguity in the structure of the S_3 state translates into a lack of consensus about the O-O bond–formation mechanism. Pulse electron paramagnetic resonance (EPR) measurements presented here conclusively resolve the oxidation state of the cofactor in the S_3 state and thus constrain the oxidation states of all S states of the cycle. The data show that the cofactor does have an expanded core topology in S_3, with all Mn ions of the cluster in the 4+ oxidation state and coordinatively saturated (six-coordinate). These results demonstrate that all S-state transitions before S_4 represent Mn-centered oxidations and provide further evidence that the O-O bond formation step is best described in terms of the coupling of two proximal Mn-bound oxygen ligands attached to Mn1 and Mn4 in the S_3 and subsequent S_4 state.

EPR spectroscopy has been extensively used to characterize the structure of the Mn_4O_5Ca cofactor and its catalytic (S state) cycle (*14, 15*).
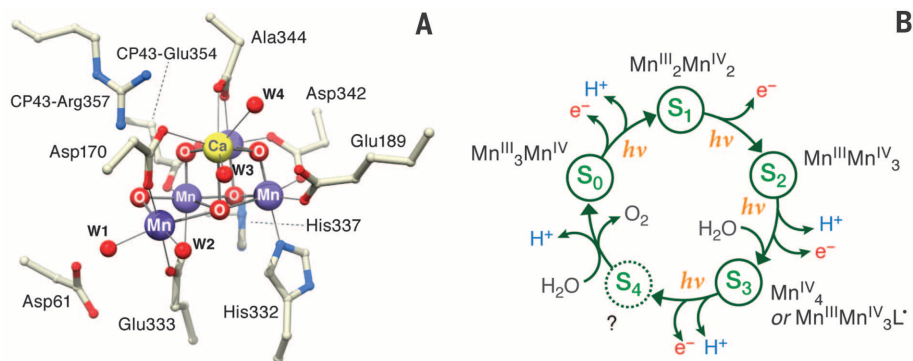
[1]Max Planck Institute for Chemical Energy Conversion, Stiftstrasse 34-36, D-45470 Mülheim an der Ruhr, Germany. [2]Institut de Biologie et de Technologies de Saclay, CNRS UMR 8221, Commissariat à l'Énergie Atomique (CEA) Saclay, 91191 Gif-sur-Yvette, France.
*Corresponding author. E-mail: nicholas.cox@cec.mpg.de (N.C.); wolfgang.lubitz@cec.mpg.de (W.L.)

Fig. 1. The water oxidation cofactor of PSII. (**A**) X-ray crystallographic structure (*7*) of the oxygen-evolving complex, a Mn_4O_5Ca cofactor. (**B**) The five intermediate "S" states of the reaction cycle (*1, 3, 33*), showing the sequence of electron- and proton-removal steps and the likely oxidation states of the Mn ions in each metastable state.

Science

A single-stranded architecture for cotranscriptional folding of RNA nanostructures

Cody Geary, Paul W. K. Rothemund and Ebbe S. Andersen

The future of RNA origami writ large

Researchers have long fabricated intricate nanostructures from carefully linked DNA strands. Now they can use RNA made by gene expression, which avoids the costly strand synthesis and lengthy annealing steps necessary with DNA origami. Geary *et al.* used molecular modeling to extend the size of folded RNA origami structures (see the Perspective by Leontis and Westhof). The modeling revealed assembly patterns for linking single-stranded RNA into A-form helices. The authors created two-dimensional structures as large as 660 nucleotides on mica surfaces.
Science, this issue p. 799; see also p. 732

ARTICLE TOOLS	http://science.sciencemag.org/content/345/6198/799
SUPPLEMENTARY MATERIALS	http://science.sciencemag.org/content/suppl/2014/08/13/345.6198.799.DC1
RELATED CONTENT	http://science.sciencemag.org/content/sci/345/6198/732.full
REFERENCES	This article cites 47 articles, 9 of which you can access for free http://science.sciencemag.org/content/345/6198/799#BIBL
PERMISSIONS	http://www.sciencemag.org/help/reprints-and-permissions

Use of this article is subject to the Terms of Service